Journal of Non-Newtonian Fluid Mechanics 198 (2013) 96–108

Contents lists available at SciVerse ScienceDirect

Journal of Non-Newtonian Fluid Mechanics

journal homepage: http://www.elsevier.com/locate/jnnfm

Some experiences with the slip boundary condition in viscous and viscoelastic flows

George Karapetsas [a], Evan Mitsoulis [b,*]

[a] Department of Mechanical Engineering, University of Thessaly, GR-38334 Volos, Greece
[b] School of Mining Engineering & Metallurgy, National Technical University of Athens, Zografou, 157 80 Athens, Greece

ARTICLE INFO

Article history:
Received 5 December 2012
Received in revised form 16 January 2013
Accepted 19 March 2013
Available online 28 May 2013

Keywords:
Slip boundary condition
Integral constitutive equations
K-BKZ model
Viscoelastic flow
Non-Newtonian fluids

ABSTRACT

A slip boundary condition (SBC) has been known to occur at solid boundaries in a variety of materials processing including polymer processing. In the present work, implementation of the SBC has been tested for viscous and viscoelastic fluids obeying integral constitutive equations of the K-BKZ type. The Finite Element Method (FEM) is used to provide numerical results for tapered dies where sometimes slip is neglected in the reservoir and the converging entry section and applied only in the die. The present results show that this is valid for small values of a dimensionless slip coefficient B_{sl} ($B_{sl} < 1$). However, slip must be applied to all the walls when $B_{sl} > 1$, or the contraction angle or the contraction ratio is small; otherwise the pressure drops in the system are severely overpredicted. Viscoelasticity enhances those trends.

1. Introduction

Slip has been known to occur at solid boundaries for a variety of materials including polymers [1]. The slip boundary condition was proposed originally by Navier [2] to take into account a non-zero velocity at solid boundaries. Although the vast majority of problems in fluid mechanics have been solved with a no-slip boundary condition, another great variety of problems has been solved with the Navier slip condition [3–6].

The works by Silliman and Scriven [7,8] were the first to apply slip at the solid boundaries for Newtonian fluids and show how this alleviates the stresses in the extrudate swell problem and reduces the swelling. In polymer processing, the work by Vlachopoulos and Hrymak [9] applied a 1-D non-linear slip model in calendering of PVC employing slip data measured experimentally. The 2-D implementation of this data was employed by Mitsoulis et al. [10] in the same problem. Since then slip has been routinely used in several problems, such as wire-coating [11], extrusion [12–16], including non-Newtonian materials such as pastes [17,18].

In polymer rheology and processing, slip has been found to occur under a wide range of conditions and it has been the subject of major research efforts, notably by Ramamurthy [19], Kalika and Denn [20], Piau's group [21–23], and Hatzikiriakos and Dealy [24–26]. Other works combine rheological measurements with numerical simulations for a polypropylene (PP) melt [27] and for a HDPE melt [28]. In the last two works the dies used were abrupt contractions, and slip was implemented at all the solid walls, namely in the reservoir and the die.

There have been arguments in the literature stating that slip is a local phenomenon occurring mostly near singularities, such as at the entrance corner in an abrupt contraction and at the exit of a die. Kamal et al. [29] assume that slip diminishes exponentially from a singularity, while in other cases only the two elements sharing the singular node employ slip [30,31]. Another assumption states that slip takes place only in the die, since shear stresses are most important there, and ignore slip on the rest of the walls [16]. However, as it will be shown in the present paper this assumption is valid only under certain conditions.

It is therefore the purpose of the present work to impose the slip boundary condition in viscous and viscoelastic flows with tapered boundaries and show the discrepancies when assuming that slip is only applied in the straight die. Furthermore, the formulation is given in some detail and results are produced for a certain viscoelastic melt (HDPE) for which experimental data is available [28].

2. Mathematical modelling

2.1. Governing equations

We consider the conservation equations of mass, momentum and energy for weakly compressible fluids under non-isothermal,

* Corresponding author. Tel.: +30 210 772 2163; fax: +30 210 772 2251.
E-mail address: mitsouli@metal.ntua.gr (E. Mitsoulis).

0377-0257/$ - see front matter © 2013 Elsevier B.V. All rights reserved.
http://dx.doi.org/10.1016/j.jnnfm.2013.03.007

creeping (Reynolds number $Re = 0$), steady flow conditions. These are written as [14,17]:

$$\bar{u}\cdot\nabla\rho+\rho(\nabla\cdot\bar{u})=0, \tag{1}$$

$$0=-\nabla p+\nabla\cdot\bar{\bar{\tau}}, \tag{2}$$

$$\rho C_p\bar{u}\cdot\nabla T=k\nabla^2T+\bar{\bar{\tau}}:\nabla\bar{u}, \tag{3}$$

where ρ is the density, $\bar{u}$ is the velocity vector, p is the pressure, $\bar{\bar{\tau}}$ is the extra stress tensor, T is the temperature, C_p is the heat capacity, and k is the thermal conductivity. For a *weakly compressible* fluid, pressure and density are connected as a first approximation through a simple linear thermodynamic equation of state [17]:

$$\rho=\rho_0(1+\beta_c p), \tag{4}$$

where β_c is the isothermal compressibility with the density to be ρ_0 at a reference pressure p_0 (=0).

The viscous stresses are given for inelastic non-Newtonian compressible fluids by the relation [14,17]:

$$\bar{\bar{\tau}}=\eta(|\dot{\gamma}|)(\bar{\bar{\dot{\gamma}}}-\frac{2}{3}(\nabla\cdot\bar{u})\bar{\bar{I}}), \tag{5}$$

where $\eta(|\dot{\gamma}|)$ is the apparent non-Newtonian viscosity, which is a function of the magnitude $|\dot{\gamma}|$ of the rate-of-strain tensor $\bar{\bar{\dot{\gamma}}}=\nabla\bar{u}+\nabla\bar{u}^T$, which is given by:

$$|\dot{\gamma}|=\sqrt{\frac{1}{2}II_{\dot{\gamma}}}=\left(\frac{1}{2}(\bar{\bar{\dot{\gamma}}}:\bar{\bar{\dot{\gamma}}})\right)^{1/2}, \tag{6}$$

where $II_{\dot{\gamma}}$ is the second invariant of $\bar{\bar{\dot{\gamma}}}$

$$II_{\dot{\gamma}}=(\bar{\bar{\dot{\gamma}}}:\bar{\bar{\dot{\gamma}}})=\sum_i\sum_j\dot{\gamma}_{ij}\dot{\gamma}_{ij}, \tag{7}$$

The tensor $\bar{\bar{I}}$ in Eq. (5) is the unit tensor.

A popular model for *purely viscous fluids* is the Cross model, which is written as [28]:

$$\eta=\frac{\eta_0}{1+(\lambda\dot{\gamma})^{1-n}}, \tag{8}$$

where η_0 is the zero-shear-rate viscosity, λ is a time constant, and n is the power-law index.

The viscosity may be dependent on temperature and pressure [1,28]. The temperature-dependence of viscosity is usually given by the Arrhenius relationship [1]:

$$a_T(T)=\frac{\eta}{\eta_0}=\exp\left[\frac{E}{R_g}\left(\frac{1}{T}-\frac{1}{T_0}\right)\right], \tag{9}$$

where α_T is the temperature-shift factor, η_0 is the zero-shear viscosity at T_0, E is the activation energy constant, R_g is the ideal gas constant, and T_0 is a reference temperature (in K).

The pressure-dependence of viscosity can be taken into account by multiplying the constitutive relation with a pressure-shift factor, a_p, defined by the Barus equation, that is [1,28]:

$$a_p\equiv\frac{\eta}{\eta_{p0}}=\exp(\beta_p p), \tag{10}$$

where η is the viscosity at absolute pressure p, η_{p0} is the viscosity at ambient pressure, and β_p is the pressure coefficient.

In the case of *viscoelastic* polymer melts, a popular rheological model for the stresses is the integral K-BKZ constitutive equation proposed by Papanastasiou et al. [32] and modified by Luo and Tanner [33]. This is written as:

$$\boldsymbol{\tau}=\frac{1}{1-\theta}\int_{-\infty}^{t}\sum_{k=1}^{N}\frac{a_k}{\lambda_k}\times\exp\left(-\frac{t-t'}{\lambda_k}\right)\frac{\alpha}{(\alpha-3)+\beta I_{C^{-1}}+(1-\beta)I_C}\left[\boldsymbol{C}_t^{-1}(t')+\theta\boldsymbol{C}_t(t')\right]dt', \tag{11}$$

where t is the current time, λ_k and a_k are the relaxation times and relaxation modulus coefficients, N is the number of relaxation modes, α and β are material constants, and I_C, I_C^{-1} are the first invariants of the Cauchy–Green tensor $\boldsymbol{C}_t$ and its inverse $\boldsymbol{C}_t^{-1}$, the Finger strain tensor. The material constant θ is given by

$$\frac{N_2}{N_1}=\frac{\theta}{1-\theta}, \tag{12}$$

where N_1 and N_2 are the first and second normal stress differences, respectively. It is noted that θ is not zero for polymer melts, which possess a non-zero second normal stress difference. Its usual range is between −0.1 and −0.2 in accordance with experimental findings [1,3].

The K-BKZ model reduces to the integral Maxwell model with an appropriate choice of parameters, namely for one relaxation mode ($N = 1$), with the parameter α set equal to a big number (say, $\alpha = 10{,}000$) and the parameter β set equal to a small number (say, $\beta = 0.001$). When the parameter $\theta = 0$, then we obtain the integral form of the Upper-Convected Maxwell (UCM) model, while when $\theta \neq 0$, we obtain a combination of the upper- and lower-convected derivatives, leading simply to the Integral Maxwell model (IMX) [34,35].

2.2. Boundary conditions

The above system of equations is closed once boundary conditions have been imposed on all boundaries (elliptic boundary-value problems at steady-state conditions) [1]. These are:

(i) Along the *walls* and in cases where there is no slip, we impose the usual no-penetration, no-slip conditions

$$\bar{u}=0. \tag{13}$$

In the case of slip at the wall, the slip boundary condition (SBC) becomes:

$$\text{(no penetration)}\quad \bar{n}\cdot\bar{u}=0, \tag{14a}$$

$$\text{(slip)}\quad \bar{t}\cdot(\bar{u}-\bar{V}_B)=\beta_{sl}(\bar{t}\bar{n}:\bar{\bar{\sigma}})^b, \tag{14b}$$

where $\bar{n}$ is the unit outward normal vector, $\bar{t}$ is the unit tangential vector in the direction of flow, $\bar{V}_B$ is the velocity of the boundary (=0 when the boundary is stationary), $\bar{\bar{\sigma}}=-p\bar{\bar{I}}+\bar{\bar{\tau}}$ is the total stress tensor, β_{sl} is a slip coefficient, and b is the slip exponent. When $b = 1$, the slip law is linear. It is convenient to write the slip law as:

$$\left[\left(\frac{\bar{t}\cdot(\bar{u}-\bar{V}_B)}{\beta_{sl}}\right)^{\frac{1}{b}}\frac{1}{(\bar{t}\cdot(\bar{u}-\bar{V}_B))}\right](\bar{t}\cdot(\bar{u}-\bar{V}_B))=(\bar{t}\bar{n}:\bar{\bar{\sigma}}), \tag{15a}$$

or

$$k_{sl}(\bar{t}\cdot(\bar{u}-\bar{V}_B))=(\bar{t}\bar{n}:\bar{\bar{\sigma}}), \tag{15b}$$

where k_{sl} is a function of the velocities in the general nonlinear case ($k_{sl} = 1/\beta_{sl}$ for a linear slip law). It is noted here that the slip law assumed is valid for all wall shear stresses (no cut-off stress value) and is not pressure-dependent because no such relation was found for the HDPE melt at hand [28]. However, if experimental data exist for a cut-off shear stress [24,36–38] or for pressure-dependence [39–41], these modifications can be easily accommodated.

(ii) Along the *centerline*, we impose symmetry conditions:

$$u_r=0,\quad \tau_{rz}=0, \tag{16}$$

where u_r is the radial component of velocity and τ_{rz} is the shear stress.

(iii) Along the *outflow boundary*, we apply the free boundary condition (FBC) [42–44] by evaluating the relevant terms of the momentum Eq. (2) and the energy Eq. (3) as follows:

$$\int_{\Gamma}(\bar{n}\cdot(-p\bar{\bar{I}}+\bar{\bar{\tau}}))d\Gamma, \tag{17a}$$

$$\int_{\Gamma}(\bar{n}\cdot\nabla T)d\Gamma, \tag{17b}$$

where Γ is the outflow boundary length.

(iv) Along the *inflow boundary*, we apply either a fully-developed velocity profile corresponding to a given flow rate Q or the free boundary condition (FBC) as modified to apply also at inlet boundaries [45].

2.3. Dimensionless groups

To make the variables dimensionless, we take as a characteristic velocity the outflow average velocity U, and as a characteristic length the die radius R. Then a characteristic apparent shear rate $\dot{\gamma}_A$ is defined as:

$$\dot{\gamma}_A=\frac{4U}{R}. \tag{18}$$

All velocities are then scaled by U, all lengths by R, and all pressures and stresses by $\bar{\eta}U/R$, where $\bar{\eta}=f(U/R)$ is a nominal viscosity given by the Cross model (Eq. (8)) at a nominal shear rate of U/R and reference temperature T_0, or for Newtonian fluids equal to a constant viscosity μ.

Viscoelasticity is usually assessed by the Weissenberg number, Ws. This is defined as:

$$Ws=\frac{\lambda U}{R}. \tag{19}$$

The pressure-dependence of the viscosity gives rise to the dimensionless pressure-shift parameter, B_p. This is defined as:

$$B_p=\frac{\beta_p\bar{\eta}U}{R}. \tag{20}$$

Similarly, the compressibility coefficient β_c gives rise to the dimensionless compressibility parameter, B_c. This is defined as:

$$B_c=\frac{\beta_c\bar{\eta}U}{R}. \tag{21}$$

The corresponding dimensionless slip parameter, B_{sl}, is a measure of fluid slip at the wall:

$$B_{sl}=\frac{\beta_{sl}\bar{\eta}^b}{U}\left(\frac{U}{R}\right)^b. \tag{22}$$

The various thermal and flow parameters are combined to give appropriate dimensionless numbers [45]. The relevant ones here are the Peclet number, Pe, and the Nahme–Griffith number, Na. These are defined as:

$$Pe=\frac{\rho C_p UR}{k}, \tag{23}$$

$$Na=\frac{\bar{\eta}EU^2}{kR_gT_0^2}. \tag{24}$$

The Pe number represents the ratio of heat convection to conduction, and the Na number represents the ratio of viscous dissipation to conduction and indicates the extent of coupling between the momentum and energy equations.

3. Method of solution

3.1. Finite element formulation

The numerical solution of the above sets of governing equations and boundary conditions has been obtained with the Finite Element Method (FEM), using two different programs. The first (called *uvpth*) has been developed and used mainly for non-Newtonian (pseudoplastic and viscoplastic) problems, for which it has been found more suitable [46]. The second (called *caves*) has been developed and used for non-Newtonian viscoelastic problems, governed by integral constitutive equations of the K-BKZ type [47,48]. Both programs employ as primary variables the two velocities, pressure, temperature and free-surface location (*u-v-p-T-h formulation*), and use a Picard (direct substitution) iterative scheme. The viscoelastic program *caves* can also accommodate purely viscous models for checking purposes against *uvpth*.

The major features of the codes are as follows. The physical domain is discretized using quadrilateral elements. The velocity vector, the temperature, and the stream function are approximated by 9-node Lagrangian basis functions, ϕ^i, and the pressure is approximated with 4-node Lagrangian basis functions, ψ^i. In the *caves* code, the 9-node Lagrangian element has been substituted by an 8-node serendipity element for faster calculations [47] (see Fig. 1).

For the governing conservation Eqs. (1)–(3), the finite element/Galerkin method is employed, which after applying the divergence theorem results in the following weak forms:

$$\int_{\Omega}[(\bar{u}\cdot\nabla\rho)+\rho(\nabla\cdot\bar{u})]\psi^i\,d\Omega=0, \tag{25}$$

$$\int_{\Omega}[(-p\bar{\bar{I}}+\bar{\bar{\tau}})\cdot\nabla\phi^i]d\Omega=\int_{\Gamma}\bar{n}\cdot(-p\bar{\bar{I}}+\bar{\bar{\tau}})\phi^i\,d\Gamma, \tag{26}$$

$$\int_{\Omega}\left[(Pe\bar{u}\cdot\nabla T)\phi^i+\nabla T\cdot\nabla\phi^i-(\bar{\bar{\tau}}:\nabla\bar{u})\phi^i\right]d\Omega=\int_{\Gamma}(\bar{n}\cdot\nabla T)\phi^i\,d\Gamma, \tag{27}$$

where $d\Omega$ and $d\Gamma$ are the differential volume and surface area, respectively. In the above, the surface integrals that appear in the right-hand side (RHS) of Eqs. (26) and (27) are applied as the free boundary conditions (FBC) [42–44] at the outflow according to:

$$\int_{\Gamma}(\bar{n}\cdot(-p\bar{\bar{I}}+\bar{\bar{\tau}}))\varphi^i d\Gamma=\underbrace{\int_{\Gamma_{FBC}}\begin{pmatrix}n_r(-p+\tau_{rr})+n_z\tau_{rz}\\ n_r\tau_{rz}+n_z(-p+\tau_{zz})\end{pmatrix}\varphi^i d\Gamma}_{\text{free boundary condition}}, \tag{28a}$$

$$\int_{\Gamma}(\bar{n}\cdot\nabla T)\phi^i d\Gamma=\underbrace{\int_{\Gamma_{FBC}}\left(n_r\frac{\partial T}{\partial r}+n_z\frac{\partial T}{\partial z}\right)\varphi^i d\Gamma}_{\text{free boundary condition}}. \tag{28b}$$

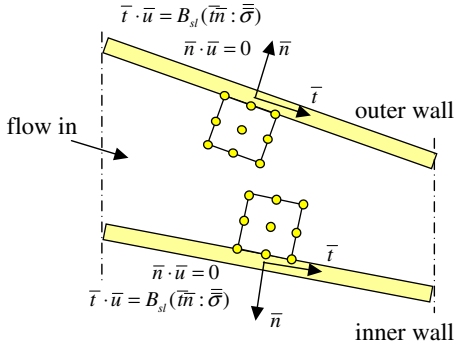

Fig. 1. The slip boundary condition along two walls. Its implementation is along the sides of the finite elements coinciding with the walls.

3.2. Implementation of the slip boundary condition (SBC) along an Inclined Wall

In past works with purely viscous [10,11,17,18] or viscoelastic models [27,28], slip was implemented making use of the rotation tensor [R], which pre- and post-multiplies the "stiffness" matrix [S] and pre-multiplies the "load" vector {B} in a Picard scheme [49]. In the present work, we adopt another approach, where the differential equations for the SBC are written explicitly. Both programs were modified to implement the SBC along the following lines.

The two equations needed are Eqs. (14a) and (14b). In an axisymmetric coordinate system (r,z,θ), one equation will give contributions to the r-component and the other to the z-component of the momentum equation.

The no penetration condition, Eq. (14a), gives at the slip wall:

$$\bar{n}\cdot\bar{u} = n_r u_r + n_z u_z = 0. \tag{29}$$

This equation will be used to replace the r-component of the momentum equation and therefore will be used for the evaluation of the radial velocity, u_r.

The z-component of the surface integral term in the momentum Eq. (26) gives at the slip wall:

$$\int_\Gamma (\bar{e}_z\cdot(\bar{n}\cdot\bar{\bar{\sigma}}))\varphi^i d\Gamma = \int_\Gamma (n_r\sigma_{rz}+n_z\sigma_{zz})\varphi^i d\Gamma. \tag{30}$$

The slip law (Eq. 15b) gives in dimensionless form:

$$K_{sl}(\bar{t}\cdot(\bar{u}-\overline{V}_B)) = (\bar{t}\bar{n}:\bar{\bar{\sigma}}), \tag{31}$$

where K_{sl} is given by:

$$K_{sl} = \left[\left(\frac{\bar{t}\cdot(\bar{u}-\overline{V}_B)}{B_{sl}}\right)^{\frac{1}{b}}\frac{1}{(\bar{t}\cdot(\bar{u}-\overline{V}_B))}\right]. \tag{32}$$

The use of K_{sl} is convenient because it employs the velocities from a previous solution. Also note that in 2-D flows, $(\bar{t}\cdot(\bar{u}-\overline{V}_B)) = (\bar{u}-\overline{V}_B) = \sqrt{(u_r-V_{Br})^2+(u_z-V_{Bz})^2}$.

In long-hand notation we have:

$$\begin{aligned} &K_{sl}(t_r(u_r-V_{Br})+t_z(u_z-V_{Bz})) \\ &\quad = [t_r(n_r\sigma_{rr}+n_z\sigma_{rz})+t_z(n_r\sigma_{rz}+n_z\sigma_{zz})]. \end{aligned} \tag{33}$$

Hence, combining Eqs. (30) and (33) yields:

$$\begin{aligned} &\int_\Gamma (\bar{e}_z\cdot(\bar{n}\cdot\bar{\bar{\sigma}}))\varphi^i d\Gamma = \\ &\int_\Gamma \left(\frac{1}{t_z}[K_{sl}(t_r(u_r-V_{Br})+t_z(u_z-V_{Bz}))]-\frac{t_r}{t_z}(n_r\sigma_{rr}+n_z\sigma_{rz})\right)\varphi^i d\Gamma. \end{aligned} \tag{34}$$

It should be noted that in the above we have for the components of the total stress $\bar{\bar{\sigma}}$:

$$\sigma_{rr} = -p + 2\frac{\partial u_r}{\partial r} + \tau_{el,rr}, \tag{35a}$$

$$\sigma_{zz} = -p + 2\frac{\partial u_z}{\partial z} + \tau_{el,zz}, \tag{35b}$$

$$\sigma_{rz} = \left(\frac{\partial u_r}{\partial z}+\frac{\partial u_z}{\partial r}\right) + \tau_{el,rz}, \tag{35c}$$

where $\bar{\bar{\tau}}_{el}$ is the elastic stress tensor with components given by Eq. (11). This occurs because with viscoelastic models, we apply the elastic-viscous split stress (EVSS) [50] (or adaptive elastic-viscous split stress, AVSS) [51], where a Newtonian contribution is added and subtracted from the extra stress tensor. Detailed information about the discrete formulation implemented in the two codes is given in the Appendix.

4. Results and discussion

4.1. Poiseuille flow of a Maxwell fluid (Test #1)

The very first test was done for simple pressure-driven (Poiseuille) flow in a tube or between flat plates for a Newtonian fluid with both codes. Fig. 2 shows the solution domain and boundary conditions, together with a 5x5 finite element grid in the understanding that if the method is correct it should work even with the sparsest of grids. By assuming both at inlet and outlet the FBC and setting the mean velocity equal to 1 at one inlet node (the centreline u_z dof), the results reproduced the analytical velocity profile everywhere and the linear pressure drop according to the well-known analytical solution for any value of B_{sl} from 0 to 1000.

We then tested the implementation of the SBC with the viscoelastic Maxwell fluid in Poiseuille flow in a tube for further code validation. The integral constitutive equation is written as [1]:

$$\boldsymbol{\tau} = \frac{1}{1-\theta}\int_{-\infty}^{t}\frac{a}{\lambda}\exp\left(-\frac{t-t'}{\lambda}\right)\left[\mathbf{C}_t^{-1}(t')+\theta\mathbf{C}_t(t')\right]dt', \tag{36}$$

where λ is a single relaxation time and a is a single relaxation modulus. Due to the presence of a non-zero θ-value, there are both first and second normal stress differences, N_1 and N_2, respectively. It is well known that in the limit of zero shear rate one must have $-1/4 \leqslant N_2/N_1 \leqslant 0$ for every fluid which climbs a rod and bulges in a tilted trough [34].

It is not difficult to obtain the analytical solution for Poiseuille flow in the presence of linear slip for the above integral Maxwell fluid with a non-zero second normal-stress difference ($\theta \neq 0$). The solution for the velocity is the same as for a Newtonian fluid:

$$(\text{axisymmetric}, r-z)\quad u_z(r) = \frac{2}{1+4B_{sl}}(1-r^2+2B_{sl}), \tag{37a}$$

$$(\text{planar}, x-y)\quad u_x(y) = \frac{3}{2(1+3B_{sl})}(1-y^2+2B_{sl}), \tag{37b}$$

while for the stresses is as follows:

$$\tau_{rr}(r) = 2Ws\left(\frac{\theta}{1-\theta}\right)\dot{\gamma}_{rz}^2,\quad \tau_{yy}(y) = 2Ws\left(\frac{\theta}{1-\theta}\right)\dot{\gamma}_{xy}^2, \tag{37c}$$

$$\tau_{zz}(r) = 2Ws\left(\frac{1}{1-\theta}\right)\dot{\gamma}_{rz}^2,\quad \tau_{xx}(y) = 2Ws\left(\frac{1}{1-\theta}\right)\dot{\gamma}_{xy}^2, \tag{37d}$$

$$\tau_{rz}(r) = \dot{\gamma}_{rz},\quad \tau_{xy}(y) = \dot{\gamma}_{xy}, \tag{37e}$$

$$\frac{dP}{dz} = -\frac{8}{1+4B_{sl}},\quad \frac{dP}{dx} = -\frac{3}{1+3B_{sl}}, \tag{37f}$$

where $\dot{\gamma}_{rz} = \partial u_z/\partial r$ ($\dot{\gamma}_{xy} = \partial u_x/\partial y$) is the shear rate. The values of the pressure gradient were derived by imposing the average velocity equal to unity. Setting $\theta = -1/3 (N_2/N_1 = -0.25)$, $Ws = 1$ and $B_{sl} = 1$, we find:

$$\begin{aligned} (\text{axisymmetric})\ u_z(1) = 0.8,\quad \tau_{rz}(1) = -0.8,\quad \tau_{rr}(1) \\ = -0.32,\quad \tau_{zz}(1) = 0.96,\quad dP/dz = -1.6 \end{aligned}$$

$$\begin{aligned} (\text{planar})\ u_x(1) = 0.75,\quad \tau_{xy}(1) = -0.75,\quad \tau_{yy}(1) \\ = -0.28125,\quad \tau_{xx}(1) = 0.84375,\quad dP/dx = -0.75 \end{aligned}$$

For $\theta = 0$ the solution of the K-BKZ model reduces to the solution of the upper-convected Maxwell (UCM) model.

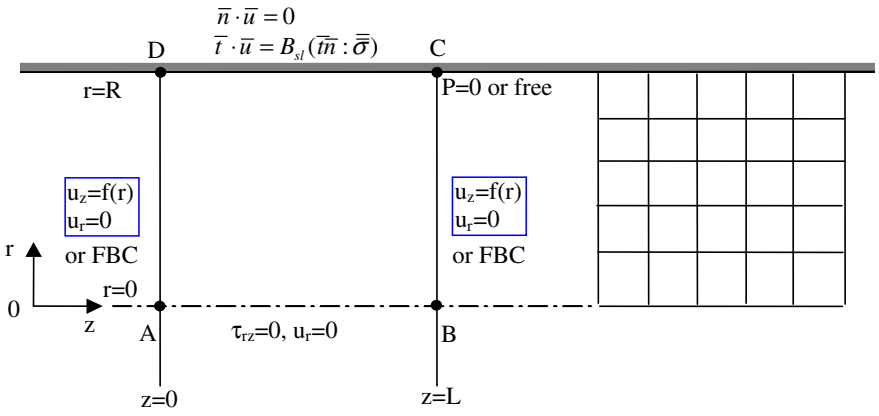

Fig. 2. Poiseuille flow in a tube. Boundary conditions and finite element grid (5 × 5). FBC stands for the free boundary condition.

The results for $Ws = 1$, $B_{sl} = 1$ and $\theta = -1/3$ are given in Fig. 3 for the contours of various flow variables, which are the pressure P, the normal stresses τ_{zz} and τ_{rr}, and the shear stress, τ_{rz}. The contours are given as 11 equidistant lines between the minimum and maximum values (not shown). We observe that all contours (except the pressure) are perfectly parallel to the flow, as they

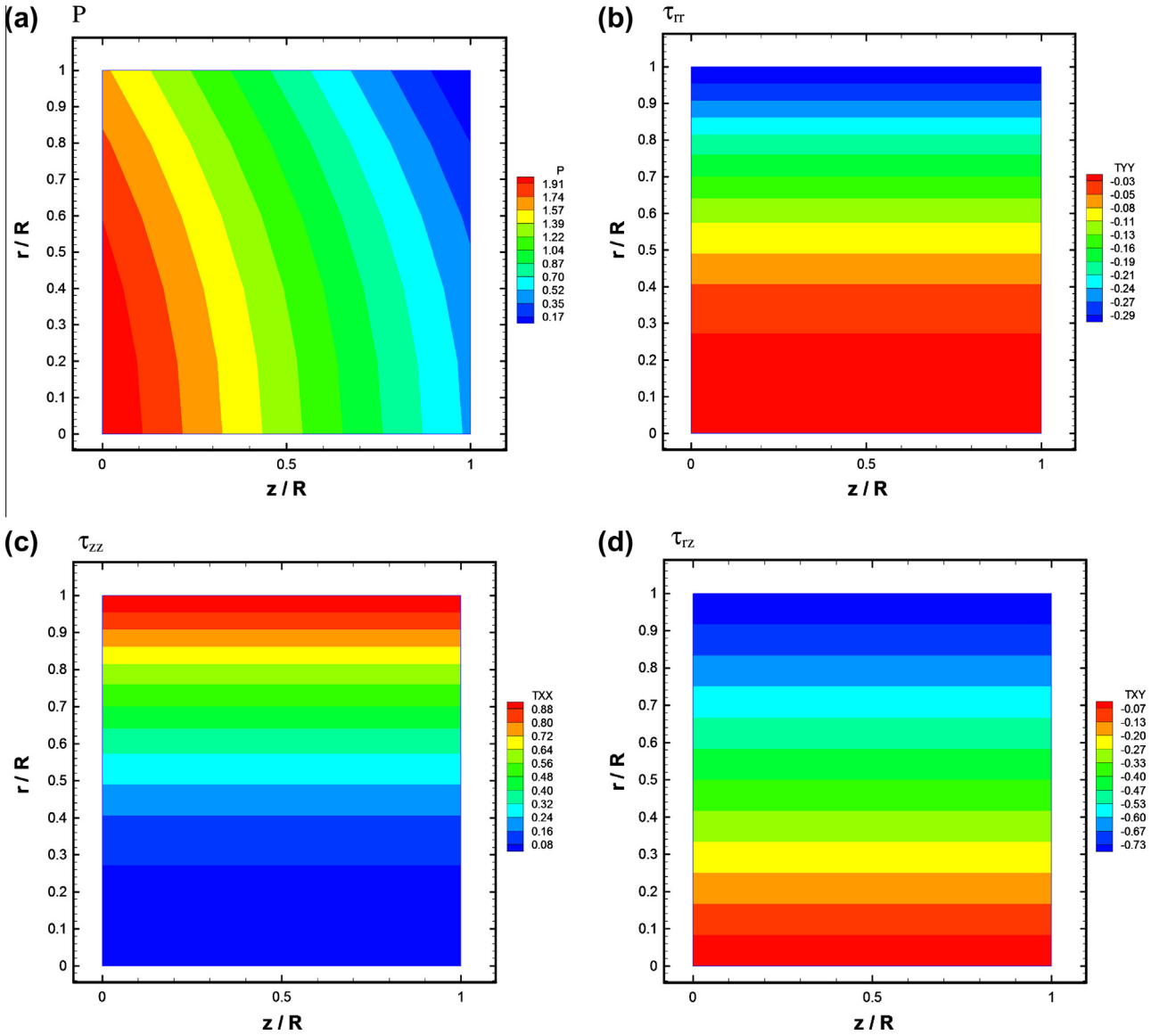

Fig. 3. Contours of field variables in Poiseuille tube flow of an integral Maxwell fluid at $Ws = 1$, $B_{sl} = 1$, $\theta = -1/3$: (a) isobars P, (b) radial stress τ_{rr}, (c) axial stress τ_{zz}, and (d) shear stress τ_{rz}.

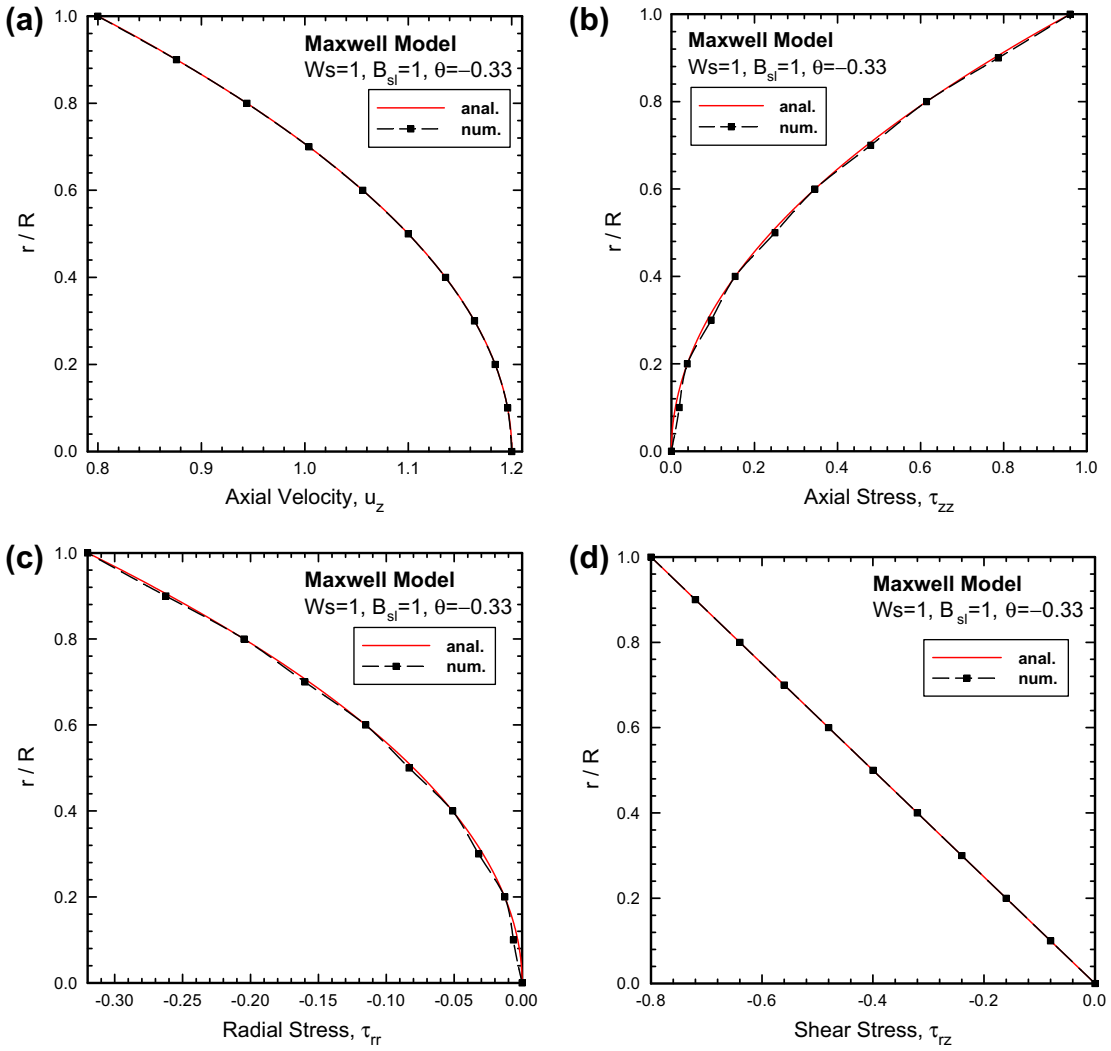

Fig. 4. Radial distributions of an integral Maxwell fluid at $Ws = 1$, $B_{sl} = 1$, $\theta = -1/3$: (a) axial velocity u_z, (b) axial stress τ_{zz}, (c) radial stress τ_{rr}, and (d) shear stress τ_{rz}. Solid lines are analytical results and symbols are numerical results.

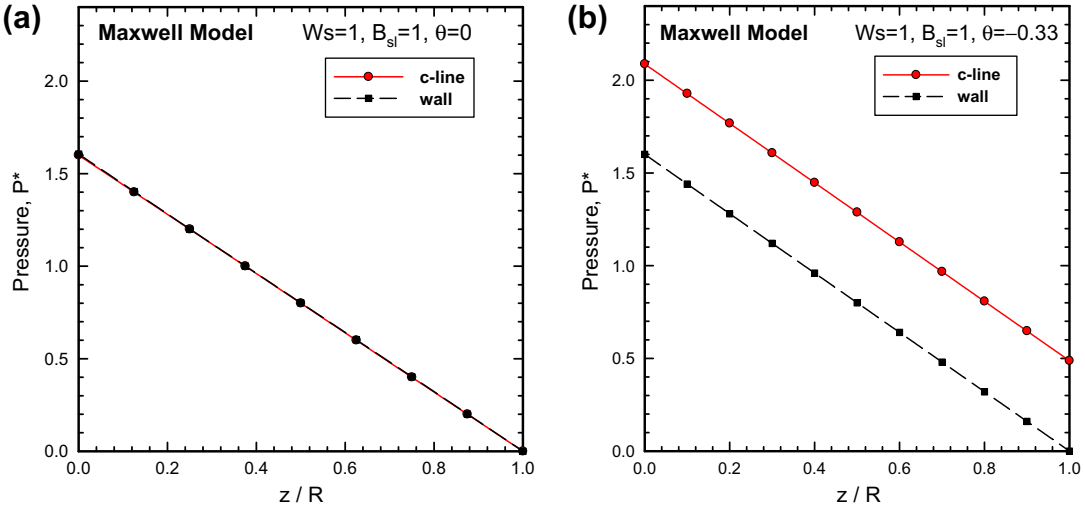

Fig. 5. Axial pressure distribution of an integral Maxwell fluid at $Ws = 1$, $B_{sl} = 1$: (a) $\theta = 0$, (b) $\theta = -1/3$.

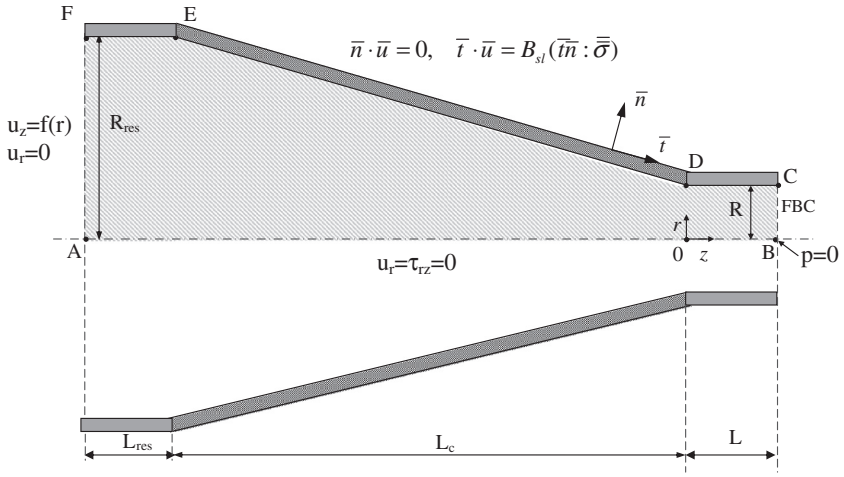

Fig. 6. Pressure-driven flow in a tapered conical die with slip at the wall. Boundary conditions at the outflow is the free boundary condition (FBC). Dimensions: $L_{res}/R = 12.5$, $L_c/R = 11.5$, $L/R = 20$, $R_{res}/R = 12.5$, $R = 0.0381$ cm. The tapered angle is then $2\phi = 90°$. D is the singular node where the taper meets the die.

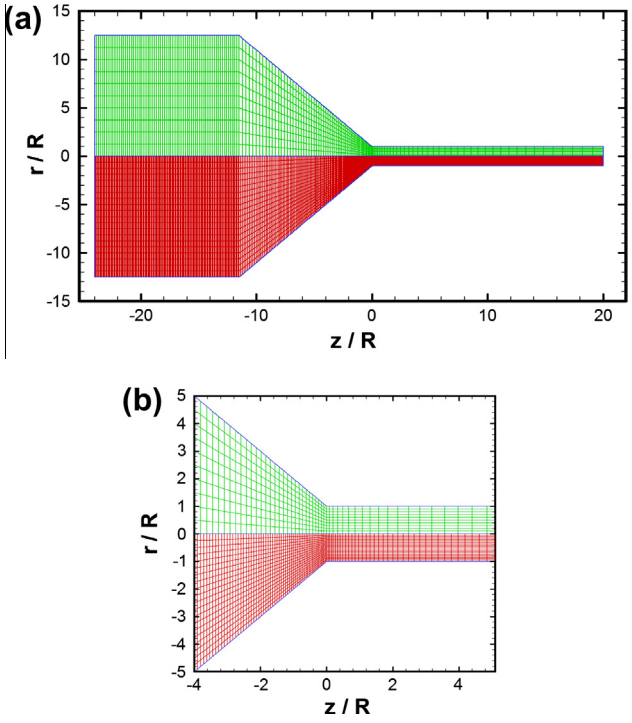

Fig. 7. (a) A typical finite element grid for the simulations in an 12.5:1 tapered circular contraction with $L/R = 20$ and $2\phi = 90°$. The upper grid (M1) consists of 1700 elements and 5461 nodes, while the lower grid is created by subdivision of each M1 element into 4 sub-elements to form a denser grid for checking the results for grid-independence and (b) detailed grids near the die entry.

should, since this is a fully-developed shear flow. The pressure contours (isobars) show the distinct curvature associated with a non-zero N_2. When $N_2 = 0$, the isobars are perfectly vertical.

Fig. 4 shows the radial distributions for the axial velocity and the stresses for $Ws = 1$, $B_{sl} = 1$ and $\theta = -1/3$. The results coincide with the analytical solutions given in Eq. (37). The axial pressure distributions of an integral Maxwell fluid at $Ws = 1$, $B_{sl} = 1$ are given in Fig. 5 for (a) $\theta = 0$ and (b) $\theta = -1/3$. In both cases, the axial pressure distribution is linear. However, when $\theta = 0$, the axial pressure distribution along the wall and the centreline coincide. When $\theta \neq 0$, there is a radial distribution of pressure, which is quadratic in r, and the results between the wall and the centreline are different. In both cases, the numerical results agree exactly with the analytical solutions of Eq. (37).

4.2. Flow of Newtonian fluids in a tapered die (Test #2)

We continue our numerical tests for a Newtonian fluid flowing under pressure in a tapered circular die making an angle ϕ of 45° with the horizontal as shown in Fig. 6 (contraction angle $2\phi = 90°$), where all the dimensions are given. D is the singular node where the taper meets the die. The choice of this simple problem is due to its use in rheometry, where several rheometrical properties are measured [52]. The boundary conditions are also shown in Fig. 6. These involve a fully developed velocity profile at inlet corresponding to a mean outflow velocity $U = 1$, and slip velocities at the solid walls ABC and FED. At outflow CD the usual practice is to put zero surface tractions $\bar{T} = 0$, since the profile is not known there. An alternative is to use the free boundary condition (FBC) [42–44]. The latter option is used in this paper.

Fig. 7 shows the finite element meshes used. The upper grid consists of 1700 elements, 5461 nodes, and 18,264 unknown degrees of freedom (d.o.f.) and was used for preliminary runs to gain experience, while a 4-times denser grid having 6800 elements was also used, having been created by subdivision of each element into 4 sub-elements for checking purposes of grid-independent results (see Fig. 7, lower half). This checking consists of reporting the overall pressures in the system from the two meshes and making sure that the differences are less than 1% between the two results.

Two runs have been made, at a low slip parameter ($B_{sl} = 1$) and a high one ($B_{sl} = 100$). For each case we have assumed slip either only along the die (*die slip*) or along the entire wall (*full slip*). The purpose here is to find out the differences when assuming slip only at the die wall [16]. How this is done with finite elements affects the results very much. We found that the best way to implement *die slip* is for the singular node D to have *both* boundary conditions, namely, to belong to the tapered wall with zero velocity for the left finite element and to belong to the die wall with slip velocity for the right finite element sharing the singular node D. If D takes only one boundary condition the results are grossly different in either case (zero velocity or slip velocity), and wiggles arise in the numerical solution.

The axial velocity profiles for $B_{sl} = 1$ are given in Fig. 8a, and these for $B_{sl} = 100$ are given in Fig. 8b. First we observe that because of slip, the velocity profiles are nowhere equal to 0. For low slip, the profiles inside the die are different along the wall

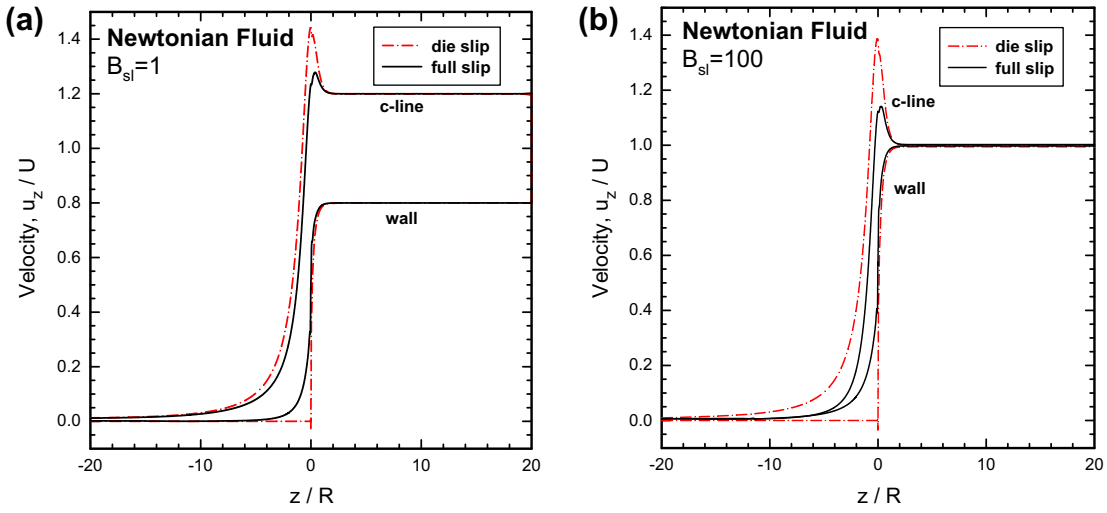

Fig. 8. Axial velocity profiles of a Newtonian fluid through a tapered conical die with a contraction ratio $R_{res}/R = 12.5$ and a tapered angle $2\phi = 90°$: (a) $B_{sl} = 1$ and (b) $B_{sl} = 100$. Results are shown when slip has been applied only in the die (die slip) and along the walls of the reservoir-tapered die-straight die (full slip).

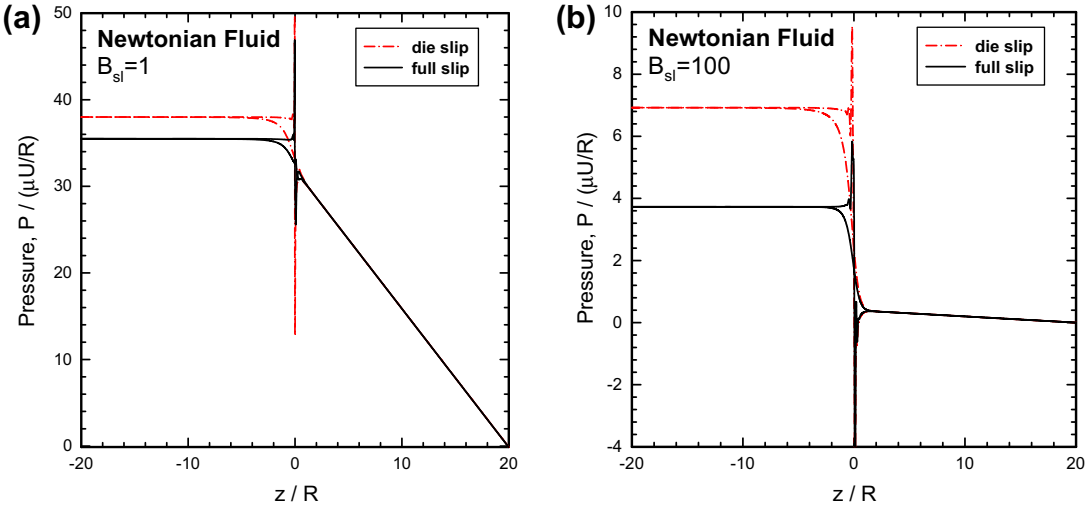

Fig. 9. Axial pressure profiles of a Newtonian fluid through a tapered conical die with a contraction ratio $R_{res}/R = 12.5$ and a tapered angle $2\phi = 90°$: (a) $B_{sl} = 1$ and (b) $B_{sl} = 100$. Results are shown when slip has been applied only in the die (die slip) and along the walls of the reservoir-tapered die-straight die (full slip).

Table 1
Parameters for the HDPE melt obeying the Cross model (Eq. (8)) at 190 °C [28].

Parameter	Value
η_0	128,180 Pa s
λ	2.8 s
n	0.227

Table 2
Values of the various parameters for the HDPE melt at 190 °C [28].

Parameter	Value
β_c	0.00095 MPa^{-1}
β_p	0.01036 MPa^{-1}
β_{sl}	70,400 cm/(s MPa^b)
b	5.73
ρ	0.7624 g/cm^3
C_p	2.7212 J/(g K)
k	0.00255 J/(s cm K)
E	28,840 J/mol
R_g	8.3143 J/(mol K)
T_0	190 °C (463 K)

and the centreline (c-line), while for high slip they tend to be virtually the same (massive slip, plug-like profiles in the die). When we compare the profiles obtained by applying partial slip only along the die (die slip, dashed lines) with those obtained by applying everywhere slip (full slip, solid lines), we observe that at low slip ($B_{sl} = 1$) there is not much difference, but at high slip ($B_{sl} = 100$) the differences before entry to the die become more pronounced, especially in the high peaks obtained just before the die entry.

The situation is more dramatic when considering the corresponding results for the pressures in Fig. 9a and b, respectively. We observe that for low slip ($B_{sl} = 1$), the pressure is overestimated by 7% ($P^* = 38$ vs. 35.6) when considering only die slip. On the other

hand, for high slip (B_{sl} = 100), the pressure is overestimated by 86% (P^* = 6.92 vs. 3.73) when considering only die slip, which is obviously not at all a good approximation. As the contraction angle 2ϕ is reduced or the contraction ratio R_{res}/R is reduced, including slip in the reservoir and the tapered entry section becomes more important, as will be shown below. Therefore, it is not warranted to include slip only at the die walls, but slip should be properly accounted for and applied along all solid walls.

4.3. Flow of a HDPE melt in a tapered die (Test #3)

We turn our attention to a flow of a polymer melt (HDPE with a polydispersity index 42 [28]) through the same tapered contraction and die used in rheometry [52]. First we present results with the viscous Cross model at two apparent shear rates $\dot{\gamma}_A = 64\ s^{-1}$ and $1000\ s^{-1}$. The flow is considered creeping ($Re \approx 0$), viscous, non-isothermal, with a pressure-dependence of the viscosity. Due

Table 3
Range of the dimensionless parameters in the flow of HDPE melt at 190 °C (die radius R = 0.0381 cm) [28].

Apparent Shear Rate, $\dot{\gamma}_A$ (s^{-1})	Peclet number, Pe	Nahme number, Na	Compressibility parameter, B_c	Pressure-shift parameter, B_p	Slip parameter, B_{sl}
64	20.8	0.02	9.8×10^{-5}	1.1×10^{-3}	0.24
1000	325.4	0.51	1.9×10^{-4}	2.1×10^{-3}	0.72

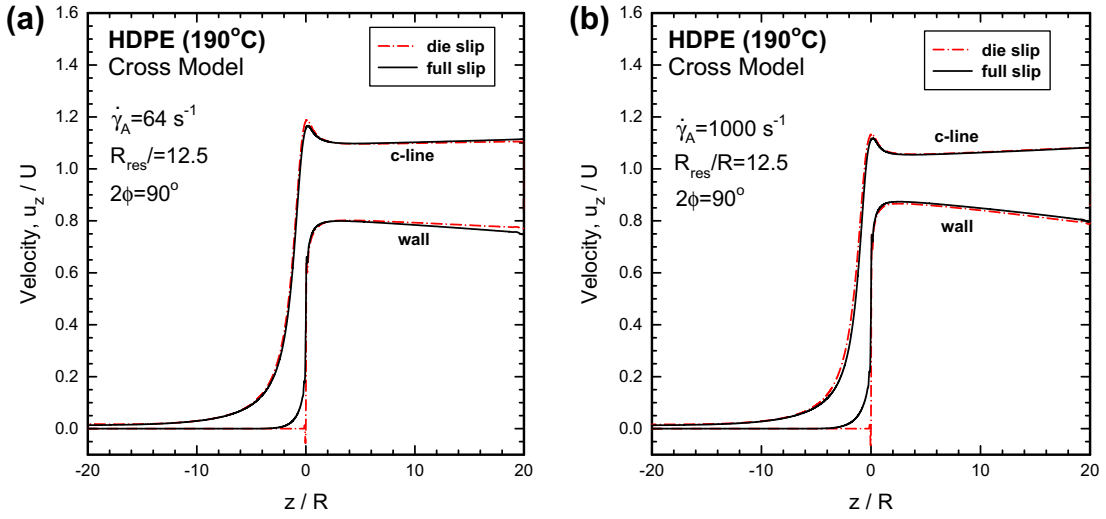

Fig. 10. Axial velocity profiles of a HDPE melt through a tapered conical die with a contraction ratio R_{res}/R = 12.5 and a tapered angle 2ϕ = 90°: (a) $\dot{\gamma}_A = 64\ s^{-1}$ and (b) $\dot{\gamma}_A = 1000\ s^{-1}$. Results obtained with the Cross model are shown when slip has been applied only in the die (die slip) and along the walls of the reservoir-tapered die-straight die (full slip).

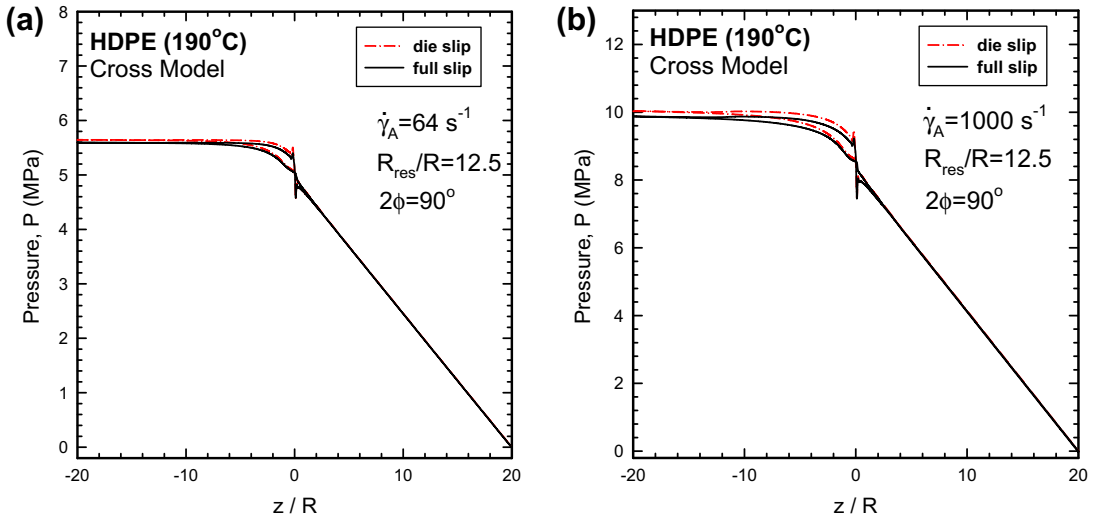

Fig. 11. Axial pressure profiles of a HDPE melt through a tapered conical die with a contraction ratio R_{res}/R = 12.5 and a tapered angle 2ϕ = 90°: (a) $\dot{\gamma}_A = 64\ s^{-1}$ and (b) $\dot{\gamma}_A = 1000\ s^{-1}$. Results obtained with the Cross model are shown when slip has been applied only in the die (die slip) and along the walls of the reservoir-tapered die-straight die (full slip).

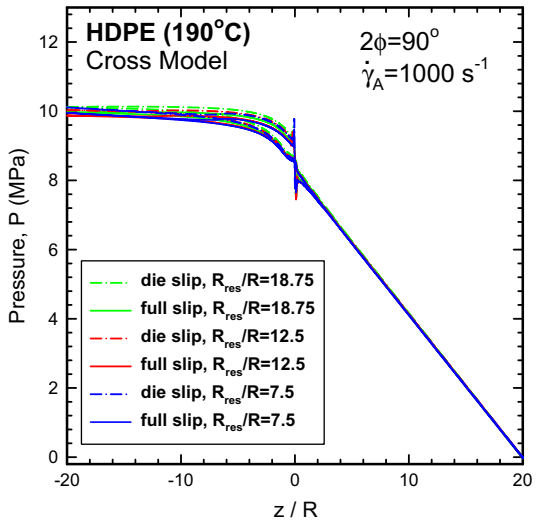

Fig. 12. The effect of contraction ratio R_{res}/R on the axial pressure profiles of a HDPE melt through a tapered conical die with a tapered angle $2\phi = 90°$ at $\dot{\gamma}_A = 1000\ s^{-1}$. Results obtained with the Cross model are shown when slip has been applied only in the die (die slip) and along the walls of the reservoir-tapered die-straight die (full slip).

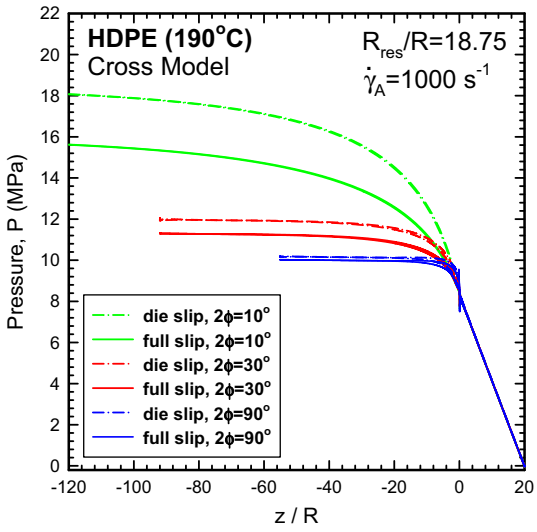

Fig. 13. The effect of contraction angle 2ϕ on the axial pressure profiles of a HDPE melt through a tapered conical die with a contraction ratio $R_{res}/R = 18.75$ at $\dot{\gamma}_A = 1000\ s^{-1}$. Results obtained with the Cross model are shown when slip has been applied only in the die (die slip) and along the walls of the reservoir-tapered die-straight die (full slip).

Table 4
Relaxation spectrum and material constants for the HDPE melt obeying the K-BKZ model (Eq. (11)) at 190 °C ($\alpha = 10.15, \beta = 0.6, \theta = 0, \bar{\lambda} = 11.3$ s, $\eta_0 = 140,073$ Pa s) [28].

k	λ_k (s)	a_k (Pa)
1	0.537×10^{-8}	0.236×10^{9}
2	0.782×10^{-5}	0.576×10^{7}
3	0.263×10^{-2}	99,508
4	0.10591	92,960
5	0.168×10^{-1}	0.104×10^{6}
6	0.70421	46,958
7	4.2105	12,169
8	30.494	1438.6

to the weak compressibility, we do not consider it here or in the following, as the results did not depend in any meaningful manner on it. The viscosity of the melt obeys the Cross model (Eq. (8)) with data listed in Table 1. Furthermore, the material slips at the wall according to a power law (Eq. (15)), and the constants β_{sl} and b are listed in Table 2 together with other material data [28]. The walls are kept isothermal at $T_0 = 190$ °C. The dimensionless variables for these two apparent shear rates are given in Table 3 (note that in [28] the dimensionless variables are slightly different as they were obtained by using $U = \dot{\gamma}_A/4$ instead of $U = \dot{\gamma}_A R/4$ as was done here). We observe that compressibility and pressure-dependence of the viscosity (B_c and B_p parameters) are not important. Also thermal effects (Pe and Na parameters) are not very important for $\dot{\gamma}_A = 64\ s^{-1}$ but they become more important for $\dot{\gamma}_A = 1000\ s^{-1}$. Finally, the slip parameter B_{sl} is 0.24 and 0.72, respectively, namely of order $O(0.1)$, which shows small slip effects.

The axial velocity profiles along the centreline (c-line) and the die walls are shown in Fig. 10a for $\dot{\gamma}_A = 64\ s^{-1}$ and in Fig. 10b for $\dot{\gamma}_A = 1000\ s^{-1}$, respectively. Due to slip at the wall, the profiles in the die have a non-zero velocity at the die wall, which becomes higher as the apparent shear rate becomes higher. However, due to the slip parameter being of O (0.1), the differences between assuming slip along all the walls (full slip) and only at the die walls (die slip) is not significant. Thus, the assumption of using slip only along the die walls for a shear-thinning polymer melt (such as the HDPE at hand) obeying the Cross model (or a similar model like the Carreau) is valid for the velocities [16].

The axial pressure profiles along the centreline (c-line) and the die walls are shown in Fig. 11a for $\dot{\gamma}_A = 64\ s^{-1}$ and in Fig. 11b for $\dot{\gamma}_A = 1000\ s^{-1}$, respectively. What was said above about the slip parameter being of $O(0.1)$, is even more valid here, where the pressure drop in the system is not greatly affected by assuming slip either along all the walls (full slip) or only at the die walls (die slip). Thus, the assumption of using slip only along the die walls for a shear-thinning polymer melt (such as the HDPE at hand) obeying the Cross (or Carreau) model is also valid for the pressures as well [16].

At this point, it is interesting to study the effects of contraction ratio R_{res}/R and contraction angle 2ϕ on the results. We have studied three contraction ratios [$R_{res}/R = 7.5, 12.5, 18.75$] and three contraction angles [$2\phi = 10°, 30°, 90°$] at the highest apparent shear rate of $\dot{\gamma}_A = 1000\ s^{-1}$. The results for the axial pressure distributions along the wall and the c-line either with die slip or full slip are given in Figs. 12 and 13, respectively. We observe that a smaller reduction ratio gives more differences in the two modes of applying slip, but this parameter is not very crucial for the present HDPE at $\dot{\gamma}_A = 1000\ s^{-1}$. Far more crucial is the effect of contraction angle, which as it becomes smaller gives more discrepancies, with the die slip overestimating appreciably the pressure drop in the system.

We turn now our attention to the viscoelastic data for the HDPE polymer melt [28]. The flow is considered creeping ($Re \approx 0$), viscoelastic (governed by the K-BKZ model, Eq. (11)), non-isothermal, with a pressure-dependence of viscosity (hence of the relaxation moduli a_k), with the viscoelastic spectrum given in Table 4. The apparent shear rates ranged from 5 to 1000 s^{-1}. Again we present results for two test runs at the intermediate apparent shear rate of 64 s^{-1} and at the highest apparent shear rate of 1000 s^{-1}. The dimensionless numbers of Table 3 are still valid.

The axial velocity profiles along the centreline (c-line) and the die walls are shown in Fig. 14a for $\dot{\gamma}_A = 64\ s^{-1}$ and in Fig. 14b for $\dot{\gamma}_A = 1000\ s^{-1}$, respectively. Similar results as in the case of the viscous Cross model computations are obtained, although the maximum after entry to the die is higher. Also, due to memory phenomena it takes a longer distance for the velocity profiles to level off. Again, due to the slip parameter being of $O(0.1)$, the differ-

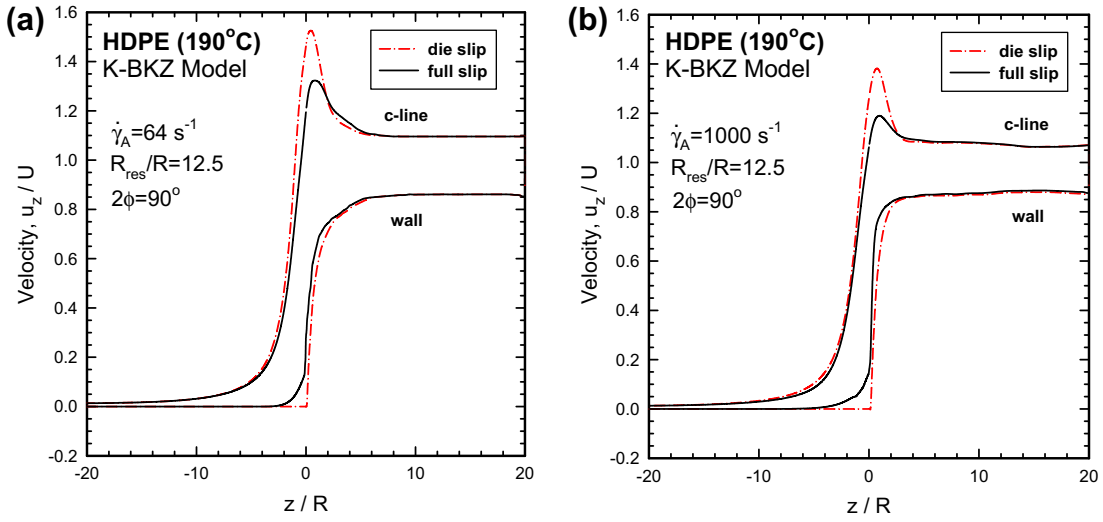

Fig. 14. Axial velocity profiles of a HDPE melt through a tapered conical die with a contraction ratio $R_{res}/R = 12.5$ and a tapered angle $2\phi = 90°$: (a) $\dot{\gamma}_A = 64\ s^{-1}$ and (b) $\dot{\gamma}_A = 1000\ s^{-1}$. Results obtained with the K-BKZ model are shown when slip has been applied only in the die (die slip) and along the walls of the reservoir-tapered die-straight die (full slip).

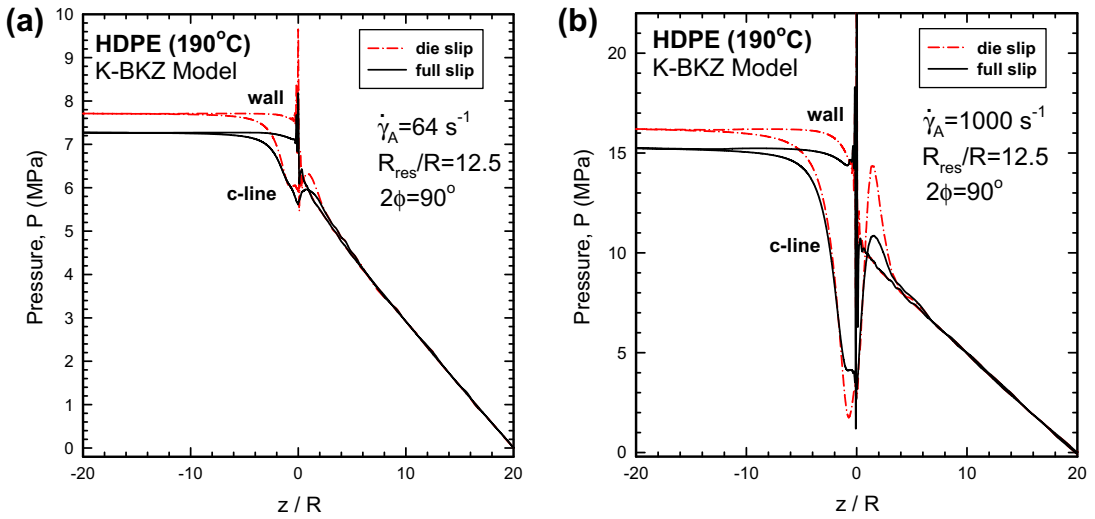

Fig. 15. Axial pressure profiles of a HDPE melt through a tapered conical die with a contraction ratio $R_{res}/R = 12.5$ and a tapered angle $2\phi = 90°$: (a) $\dot{\gamma}_A = 64\ s^{-1}$ and (b) $\dot{\gamma}_A = 1000\ s^{-1}$. Results obtained with the K-BKZ model are shown when slip has been applied only in the die (die slip) and along the walls of the reservoir-tapered die-straight die (full slip).

ences between assuming slip along all the walls (full slip) and only at the die walls (die slip) is not significant. Thus, the assumption of using slip only along the die walls for a viscoelastic polymer melt (such as the HDPE at hand) obeying the K-BKZ model is valid for the velocities [16].

The axial pressure profiles along the centreline (c-line) and the die walls are shown in Fig. 15a for $\dot{\gamma}_A = 64\ s^{-1}$ and in Fig. 15b for $\dot{\gamma}_A = 1000\ s^{-1}$, respectively. What was said above about the slip parameter being of $O(0.1)$ is still valid here, where the pressure drop in the system are somewhat affected by assuming slip either along all the walls (full slip) or only at the die walls (die slip). We observe that for $\dot{\gamma}_A = 64\ s^{-1}$, the pressure is overestimated by 5% (P = 7.3 vs. 7.7 MPa) when considering only die slip. Also, for $\dot{\gamma}_A = 1000\ s^{-1}$, the pressure is overestimated by 6% ($P = 15.3$ vs. 16.2 MPa). Thus, the assumption of using slip only along the die walls for a viscoelastic polymer melt (such as the HDPE at hand) obeying the K-BKZ model is also valid for the pressures as well [16].

5. Conclusions

The slip boundary condition (SBC) has been implemented in cases of viscous and viscoelastic flows obeying an integral constitutive equation of the K-BKZ type. The details of implementation have been given in the general case of geometries where an arbitrary angle is present. It is shown that when the dimensionless slip parameter B_{sl} is of order $O(1)$ or less, it is justified to apply the SBC only in the die, for capillary dies used in rheometry. However, when B_{sl} is of order $O(10)$ or more, this assumption is not valid and leads to gross overestimations of the pressure drop in the system. This is more so when the contraction angle or the contraction ratio are reduced.

A test case of a polymer melt (HDPE) exhibiting slip was studied, seen either as a viscous (Cross) fluid or a viscoelastic (K-BKZ) fluid. Due to the slip parameter B_{sl} being of order $O(0.1)$, it was found that the assumption of applying only slip at the die is a valid approximation, as was done before [16]. However, there are situa-

tions where B_{sl} is of order $O(10)$ or more (e.g., in wire coating or with polymers exhibiting linear slip), and then slip must be applied to all solid walls to obtain reliable results, especially for the pressures in the system, which are important in rheometry. The latter can also influence slip according to experimental evidence of pressure-dependence slip law [39,40], which can also influence flow stability [41].

Acknowledgements

The authors would like to acknowledge the financial support by the "THALES" project (subproject "COVISCO") of the Ministry of Education, Greece.

Appendix A

Our recent work [43] contains detailed derivations of the FEM formulation based on the "stiffness" matrix and "load" vector approach advocated by Huebner and Thornton [49]. Here we concentrate on the appropriate modifications to incorporate the SBC for viscoelastic models in the general case of arbitrary geometries.

A.1. Mass and momentum discrete equations

Combining the discrete forms of the conservation equations of mass and momentum (including compressibility) into one matrix equation leads (in two-dimensional axisymmetric domains, $r-z-\theta$ corresponding to 1–2–3) to the following system of an element (stiffness) matrix [S], a vector of unknowns {x}, and a RHS (load) vector {F} for each element:

$$\begin{bmatrix} S_{11} & S_{12} & S_{13} \\ S_{21} & S_{22} & S_{23} \\ S_{31} & S_{32} & S_{33} \end{bmatrix} \begin{bmatrix} \overline{U} \\ \overline{V} \\ \overline{P} \end{bmatrix} = \begin{bmatrix} \overline{F}_1 \\ \overline{F}_2 \\ 0 \end{bmatrix}. \tag{A.1}$$

The entries for each term in the above system are given in detail in [43]. The bars over U, V, P, F_1, F_2 denote arrays having the nodal values of the element.

A.2. Contribution from the SBC

With the SBC, the extra terms along the slip boundary are:

$$\overline{F}_r = \underbrace{\int_{\Gamma_{SBC}} (\bar{n}\cdot\bar{u})\bar{\varphi}\varepsilon d\Gamma}_{\text{no penetration condition}} = \underbrace{\int_{\Gamma_{SBC}} (n_r u_r + n_z u_z)\varphi^i \varepsilon d\Gamma}_{\text{no penetration condition}}, \quad i=1,3, \tag{A.2}$$

$$\overline{F}_z = \underbrace{\int_{\Gamma_{SBC}} (\bar{e}_z\cdot(\bar{n}\cdot\bar{\bar{\sigma}}))\bar{\varphi} d\Gamma}_{\text{slip boundary condition}} = \underbrace{\int_{\Gamma_{SBC}} (n_r\sigma_{rr} + n_z\sigma_{rz})\varphi^i d\Gamma}_{\text{slip boundary condition}}, \quad i=1,3, \tag{A.3}$$

where ε is a big number ($\varepsilon = 10^{+12}$) employed for a penalty-method implementation of the no-penetration condition across the slip boundary. The above terms do not enter as such in the RHS load vector {F}, but they can be split into contributions to the stiffness matrix [S] and the load vector {F}. Note that any contribution to [S] has more power numerically than in {F}, and for a linear slip law and a Newtonian fluid it requires no iterations.

After the appropriate manipulations, the following matrix system is obtained from the slip contribution:

$$\begin{bmatrix} S_{S11} & S_{S12} & S_{S13} \\ S_{S21} & S_{S22} & S_{S23} \end{bmatrix} \begin{bmatrix} \overline{U} \\ \overline{V} \\ \overline{P} \end{bmatrix} = \begin{bmatrix} \overline{F}_{S1} \\ \overline{F}_{S2} \end{bmatrix}, \tag{A.4}$$

where the components of the element (stiffness) matrix [S_S] of Eq. (A.4) are:

$$S_{S11} = \int_\Gamma (n_r\varphi^j)\varphi^i\varepsilon d\Gamma, \quad i=1,3, \quad j=1,9, \tag{A.5}$$

$$S_{S12} = \int_\Gamma (n_z\varphi^j)\varphi^i\varepsilon d\Gamma, \quad i=1,3, \quad j=1,9, \tag{A.6}$$

$$S_{S13} = 0, \tag{A.7}$$

$$\begin{aligned} S_{S21} = {} & \int_\Gamma K_{sl}\frac{t_r}{t_z}\varphi^j\varphi^i d\Gamma - \int_\Gamma \left(\frac{t_r}{t_z}n_r 2\eta_{ref}\frac{\partial\varphi^j}{\partial r}\right)\varphi^i d\Gamma \\ & - \int_\Gamma \left(\frac{t_r}{t_z}n_z\eta_{ref}\frac{\partial\varphi^j}{\partial z}\right)\varphi^i d\Gamma \\ & + \int_\Gamma \left(\frac{t_r}{t_z}n_r\frac{2\eta_{ref}}{3}\left(\frac{\partial\varphi^j}{\partial r}+\frac{\varphi^j}{r}\right)\right)\varphi^i d\Gamma, \quad i \\ & = 1,3, j=1,9 \ (4^{\text{th}} \text{ term} = 0 \text{ for incomp. fluids}), \end{aligned} \tag{A.8}$$

$$\begin{aligned} S_{S22} = {} & \int_\Gamma K_{sl}\varphi^j\varphi^i d\Gamma - \int_\Gamma \left(\frac{t_r}{t_z}n_z\eta_{ref}\frac{\partial\varphi^j}{\partial r}\right)\varphi^i d\Gamma \\ & + \int_\Gamma \left(\frac{t_r}{t_z}n_r\frac{2\eta_{ref}}{3}\frac{\partial\varphi^j}{\partial z}\right)\varphi^i d\Gamma, \quad i \\ & = 1,3, \quad j=1,9 \ (3^{\text{rd}} \text{ term} = 0 \text{ for incomp. fluids}), \end{aligned} \tag{A.9}$$

$$S_{S23} = -\int_\Gamma \frac{t_r}{t_z}n_r\psi^j\varphi^i d\Gamma, \quad i=1,3, \quad j=1,4. \tag{A.10}$$

In the above, the tangential and normal components of the unit vector are readily available in FEM from the shape functions and their derivatives.

The above contributions of [S_S] and [F_S] must be added to the corresponding terms of Eq. (A.1) for the elements having the SBC on one side.

For the integral constitutive equation (Eq. (11)), the SBC enters the RHS or "load" vector [F_S] according to (and in the general case where the boundary moves with a velocity V_B):

$$\overline{F}_{S1} = \int_\Gamma K_{sl}V_{Br}\varphi^i d\Gamma, \quad i=1,3 \tag{A.11}$$

$$\overline{F}_{S2} = \int_\Gamma K_{sl}V_{Bz}\varphi^i d\Gamma + \int_\Gamma \frac{t_r}{t_z}(n_z\sigma_{rz} + n_r\sigma_{rr})\varphi^i d\Gamma, \quad i=1,3, \tag{A.12}$$

where the total stresses σ_{rz} and σ_{rr} are given by:

$$\sigma_{rz} = \eta_{ref}\left(\frac{\partial u_z}{\partial r}+\frac{\partial u_r}{\partial z}\right) + \underbrace{\tau_{rz,el} - \eta_{ref}\left(\frac{\partial u_z}{\partial r}+\frac{\partial u_r}{\partial z}\right)}_{F_{z,el}}, \tag{A.13}$$

$$\sigma_{rr} = 2\eta_{ref}\frac{\partial u_r}{\partial r} + \underbrace{\tau_{rr,el} - 2\eta_{ref}\frac{\partial u_r}{\partial r}}_{F_{z,el}}. \tag{A.14}$$

In the above, $V_{B,r}$ and $V_{B,z}$ are the velocity components of the moving boundary (=0 if the boundary is not moving). The case of a moving boundary has been dealt with before in the process of calendering [10] and wire coating [11].

References

[1] R.I. Tanner, Engineering Rheology, seconnd ed., Oxford University Press, Oxford, 2000.
[2] C.L.M.H. Navier, Sur les lois du mouvement des fluides, Mem. Acad. Roy. Sci. Inst. Fr. 6 (1827) 389–440.
[3] R.B. Bird, R.C. Armstrong, O. Hassager, Dynamics of Polymeric Liquids, Fluid Mechanics, second ed., vol. I, Wiley, New York, 1987.
[4] D.G. Baird, D.I. Collias, Polymer Processing: Principles and Design, Butterworth-Heinemann, Boston, MA, 1995.
[5] Z. Tadmor, C.G. Gogos, Principles of Polymer Processing, SPE Monograph Series, second ed., Wiley, New York, 2006.
[6] S.G. Hatzikiriakos, Appropriate boundary conditions in the flow of molten polymers, Int. Polym. Proc. 25 (2010) 55–62.

[7] W.J. Silliman, L.E. Scriven, Slip of liquid inside a channel exit, Phys. Fluids 21 (1978) 2115–2116.
[8] W.J. Silliman, L.E. Scriven, Separating flow near a static contact line: slip at a wall and shape of a free surface, J. Comput. Phys. 34 (1980) 287–313.
[9] J. Vlachopoulos, A.N. Hrymak, Calendering poly(vinyl chloride): theory and experiments, Polym. Eng. Sci. 20 (1980) 725–731.
[10] E. Mitsoulis, J. Vlachopoulos, F.A. Mirza, Calendering analysis without the lubrication approximation, Polym. Eng. Sci. 25 (1985) 6–18.
[11] E. Mitsoulis, Finite element analysis of wire coating, Polym. Eng. Sci. 26 (1986) 171–186.
[12] N. Phan-Thien, Influence of wall slip on extrudate swell: a boundary element investigation, J. Non-Newtonian Fluid Mech. 26 (1988) 327–340.
[13] H.E.H. Meijer, C.P.J.M. Verbraak, Modeling of extrusion with slip boundary conditions, Polym. Eng. Sci. 28 (1988) 758–772.
[14] G.C. Georgiou, M.J. Crochet, Compressible viscous flow in slits, with slip at the wall, J. Rheol. 38 (1994) 639–654.
[15] G.C. Georgiou, M.J. Crochet, Time-dependent compressible extrudate-swell problem with slip at the wall, J. Rheol. 38 (1994) 1745–1755.
[16] G.C. Georgiou, The time-dependent, compressible Poiseuille and extrudate-swell flows of a Carreau fluid with slip at the wall, J. Non-Newtonian Fluid Mech. 109 (2003) 93–114.
[17] E. Mitsoulis, S.G. Hatzikiriakos, Steady flow simulations of compressible PTFE paste extrusion under severe wall slip, J. Non-Newtonian Fluid Mech. 157 (2009) 26–33.
[18] H.A. Ardakani, E. Mitsoulis, S.G. Hatzikiriakos, Thixotropic flow of toothpaste through extrusion dies, J. Non-Newtonian Fluid Mech. 166 (2011) 1262–1271.
[19] A.V. Ramamurthy, Wall slip in viscous fluids and influence of materials of construction, J. Rheol. 30 (1986) 337–357.
[20] D.S. Kalika, M.M. Denn, Wall slip and extrudate distortion in linear low-density polyethylene, J. Rheol. 31 (1987) 815–834.
[21] N. El Kissi, J.M. Piau, The different capillary flow regimes of entangled polydimethylsiloxane polymers: macroscopic slip at the wall, hysteresis and cork flow, J. Non-Newtonian Fluid Mech. 37 (1990) 55–94.
[22] J.-M. Piau, N. El-Kissi, Measurement and modelling of friction in polymer melts during macroscopic slip at the wall, J. Non-Newtonian Fluid Mech. 54 (1994) 121–142.
[23] J.-M. Piau, N. El-Kissi, A. Mezghani, Slip flow of polybutadiene through fluorinated dies, J. Non-Newtonian Fluid Mech. 59 (1995) 11–30.
[24] S.G. Hatzikiriakos, J.M. Dealy, Wall slip of molten high density polyethylenes. I. Sliding plate rheometer studies, J. Rheol. 35 (1991) 497–523.
[25] S.G. Hatzikiriakos, J.M. Dealy, Wall slip of molten high density polyethylenes. II. Capillary rheometer studies, J. Rheol. 36 (1992) 703–741.
[26] S.G. Hatzikiriakos, J.M. Dealy, Role of slip and fracture in the oscillating flow of HDPE in a capillary, J. Rheol. 36 (1992) 845–884.
[27] E. Mitsoulis, I.B. Kazatchkov, S.G. Hatzikiriakos, The effect of slip in the flow of a branched PP polymer: experiments and simulations, Rheol. Acta 44 (2005) 418–426.
[28] M. Ansari, S.G. Hatzikiriakos, E. Mitsoulis, Slip effects in HDPE flows, J. Non-Newtonian Fluid Mech. 167–168 (2012) 18–29.
[29] M.R. Kamal, S.K. Goyal, E. Chu, Simulation of injection mold filling of viscoelastic polymer with fountain flow, AIChE J. 34 (1988) 94–105.
[30] S.F. Kistler, L.E. Scriven, Coating flows, in: J.R.A. Pearson, S.M. Richardson (Eds.), Computational Analysis of Polymer Processing, Appl. Science, London, 1984, pp. 243–299.
[31] K.N. Christodoulou, L.E. Scriven, Discretization of free surface flows and other moving boundary problems, J. Compos. Phys. 99 (1992) 39–55.
[32] A.C. Papanastasiou, L.E. Scriven, C.W. Macosko, An integral constitutive equation for mixed flows: viscoelastic characterization, J. Rheol. 27 (1983) 387–410.
[33] X.-L. Luo, R.I. Tanner, Finite element simulation of long and short circular die extrusion experiments using integral models, Int. J. Numer. Methods Eng. 25 (1988) 9–22.
[34] M. Renardy, Y. Renardy, Stability of shear flows of viscoelastic fluids under perturbations perpendicular to the plane of flow, J. Non-Newtonian Fluid Mech. 32 (1989) 145–155.
[35] M. Beaulne, E. Mitsoulis, The effect of viscoelasticity in the film-blowing process, J. Appl. Polym. Sci. 105 (2007) 2098–2112.
[36] S.G. Hatzikiriakos, I.B. Kazatchkov, D. Vlassopoulos, Interfacial phenomena in the capillary extrusion of metallocene polyethylenes, J. Rheol. 41 (1997) 1299–1316.
[37] S.Q. Wang, P.A. Drda, Superfluid-like stick–slip transition in capillary flow of linear polyethylene. 1. General features, Macromolecules 29 (1996) 2627–2632.
[38] S.Q. Wang, P.A. Drda, Stick-slip transition in capillary flow of linear polyethylene. 3. Surface conditions, Rheol. Acta 36 (1997) 128–134.
[39] T.J. Person, M.M. Denn, The effect of die materials and pressure-dependent slip on the extrusion of linear low-density polyethylene, J. Rheol. 41 (1997) 249–265.
[40] H.S. Tang, D.M. Kalyon, Unsteady circular tube flow of compressible polymeric liquids subject to pressure-dependent wall slip, J. Rheol. 52 (2008) 507–525.
[41] H.S. Tang, D.M. Kalyon, Time-dependent tube flow of compressible suspensions subject to pressure dependent wall slip: ramifications on development of flow instabilities, J. Rheol. 52 (2008) 1069–1090.
[42] T.C. Papanastasiou, N. Malamataris, K. Ellwood, A new outflow boundary condition, Int. J. Numer. Methods Fluids 14 (1992) 587–608.
[43] E. Mitsoulis, N.A. Malamataris, Free (open) boundary condition: some experiences with viscous flow simulations, Int. J. Numer. Methods Fluids 68 (2012) 1299–1323.
[44] E. Mitsoulis, N.A. Malamataris, The free (open) boundary condition with integral constitutive equations, J. Non-Newtonian Fluid Mech. 177–178 (2012) 97–108.
[45] Y. Dimakopoulos, G. Karapetsas, N.A. Malamataris, E. Mitsoulis, The free (open) boundary condition at inflow boundaries, J. Non-Newtonian Fluid Mech. 187–188 (2012) 16–31.
[46] A. Hannachi, E. Mitsoulis, Sheet coextrusion of polymer solutions and melts: comparison between simulation and experiments, Adv. Polym. Technol. 12 (1993) 217–231.
[47] X.-L. Luo, E. Mitsoulis, An efficient algorithm for strain history tracking in finite element computations of non-Newtonian fluids with integral constitutive equations, Int. J. Num. Meth. Fluids 11 (1990) 1015–1031.
[48] G. Barakos, E. Mitsoulis, Non-isothermal viscoelastic simulations of extrusion through dies and prediction of the bending phenomenon, J. Non-Newtonian Fluid Mech. 62 (1996) 55–79.
[49] K.M. Huebner, E.A. Thornton, The Finite Element Method for Engineers, Wiley, New York, 1982.
[50] M.G.N. Perera, K. Walters, Long-range memory effects in flows involving abrupt changes in geometry. Part I. Flows associated with L-shaped and T-shaped geometries, J. Non-Newtonian Fluid Mech. 2 (1977) 49–81. 1977.
[51] J. Sun, N. Phan-Thien, R.I. Tanner, An adaptive viscoelastic stress splitting scheme and its applications: AVSS/SI and AVSS/SUPG, J. Non-Newtonian Fluid Mech. 65 (1996) 75–91.
[52] M. Ansari, Th. Zisis, S.G. Hatzikiriakos, E. Mitsoulis, Capillary flow of low-density polyethylene, Polym. Eng. Sci. 52 (2012) 649–662.